

Full Length Article

Determination of the absolute adsorption/desorption isotherms of CH₄ and n-C₄H₁₀ on shale from a nano-scale perspectiveYueliang Liu^a, Huazhou Andy Li^{a,b,*}, Yuanyuan Tian^{b,c}, Zhehui Jin^a, Hucheng Deng^{b,c}^a School of Mining and Petroleum Engineering, Faculty of Engineering, University of Alberta, Edmonton T6G1H9, Canada^b State Key Laboratory of Oil and Gas Reservoir Geology and Exploitation (Chengdu University of Technology), Chengdu 610059, Sichuan, PR China^c College of Energy Resources, Chengdu University of Technology, Chengdu 610059, PR China

ARTICLE INFO

Keywords:

Density of the adsorption phase
 Absolute adsorption/desorption isotherms
 Hysteresis phenomenon
 Grand Canonical Monte Carlo simulations
 Thermogravimetric analysis

ABSTRACT

Accurate description of absolute adsorption/desorption behavior for hydrocarbons on shale is of critical importance to the understanding of the fundamental mechanisms governing the storage, transport, and recovery of shale gas or shale gas condensate in shale reservoirs. By applying a thermogravimetric method, we first measure the excess adsorption/desorption isotherms of pure CH₄ and n-C₄H₁₀ on shale samples over the temperature range of 303.15–393.15 K. The maximum test pressures considered for CH₄ and n-C₄H₁₀ are 50 bar and 2 bar, respectively. Grand Canonical Monte Carlo (GCMC) simulations are then applied to calculate the density of the adsorption phase by considering the fluid-pore surface interactions. We use such calculated density of the adsorption phase to calibrate the excess adsorption/desorption isotherms, which enables us to eventually obtain the absolute adsorption/desorption isotherms. Such approach for estimating the density of the adsorption phase is essentially different from the commonly used approaches in which the density of the adsorption phase is considered to be independent of temperature, pressure, and pore size.

The adsorption/desorption test results show that both CH₄ and n-C₄H₁₀ exhibit more adsorption as temperature decreases or pressure increases. Their adsorption/desorption isotherms exhibit hysteresis phenomenon and this phenomenon weakens as temperature increases. Comparatively, the hysteresis behavior observed for n-C₄H₁₀ is more obvious than that for CH₄. Compared with CH₄, n-C₄H₁₀ has higher adsorption capacity under the same condition, indicating its higher affinity towards the shale with organic matters. As for the conventional approaches, the density calculated from the van der Waals constant *b* or the liquid hydrocarbon density can be used to reasonably well evaluate the absolute adsorption isotherms of n-C₄H₁₀ on shale, but tends to underestimate the absolute adsorption of CH₄ on shale. GCMC simulations show that the density of the adsorption phase is strongly correlated with system pressure, temperature, and pore size. Compared to the conventional approaches, GCMC simulations can better capture the *in-situ* density of adsorption phase; on the basis of the *in-situ* density of adsorption phase, we can then achieve more accurate determination of the absolute adsorption isotherms of a given hydrocarbon on shale. This study raises the imperativeness of leveraging more sophisticated simulation tools (such as GCMC) for more accurate determination of absolute adsorption isotherms.

1. Introduction

Shale resources (such as shale gas or shale gas condensate) have emerged as a key energy resource in recent years. Shale rocks generally have higher total organic carbon (TOC) content than the conventional ones, resulting in hydrocarbons being more apt to adsorb on shale surface [1]. Thereof, a significant proportion of reserves in shale reservoirs can be in the adsorbed state. During the production of shale gas or shale gas condensate, desorption plays an important role. Adsorption/desorption of hydrocarbons usually exhibits an interesting

phenomenon of hysteresis, and the knowledge about the adsorption/desorption behavior of hydrocarbons in shale is crucial for estimating the hydrocarbon storage capacity and understanding the mechanisms of the subsequent hydrocarbon recovery.

Adsorbed hydrocarbons can account for 20–85 vol% of the total reserves in shale reservoirs [2]. Many previous researches focused on investigating the adsorption capacity of hydrocarbons on shale rocks [3–5]. CH₄, known to be the most abundant component in shale gas reservoirs, was mostly studied. Some heavier hydrocarbons, e.g., C₂H₆, C₃H₈, and n-C₄H₁₀, can be also present with a large quantity in shale

* Corresponding author at: School of Mining and Petroleum Engineering, Faculty of Engineering, University of Alberta, Edmonton T6G1H9, Canada.
 E-mail address: huazhou@ualberta.ca (H.A. Li).

reservoirs, up to 20 vol% [6]. But adsorptions of these heavier components in shale rocks are scarcely measured in the literature. Pedram et al. (1984) [7] measured the adsorption isotherms of C_2H_6 , C_3H_8 , and $n-C_4H_{10}$ in two oil-shale samples and found that $n-C_4H_{10}$ has the highest adsorption capacity, followed by C_3H_8 and C_2H_6 . But it is noted that the oil-shale they used still have residual oil left in the samples, which can affect the gas adsorption on shale due to the large solubility of various hydrocarbons in shale oil. Therefore, such measured adsorption isotherms could not represent the actual adsorption capacity of gases on shale. Recently, Wang et al. (2015) [6] measured the excess adsorption isotherms of pure CH_4 and C_2H_6 on shale samples. C_2H_6 is shown to have a higher adsorption capacity than CH_4 , and Wang et al. (2015) [6] attributed this finding to that C_2H_6 is more apt to get adsorbed on shale samples than CH_4 . But this conclusion is made based on the measured excess adsorption isotherms, rather than the absolute adsorption isotherms; excess adsorption isotherms are generally not accurate enough as it neglects the adsorbed-phase volume occupied by the adsorbed gas.

By knowing the pore volume from the helium adsorption, volumetric method is commonly used to measure the adsorption isotherms of hydrocarbons on shale samples [8,9]. Recently, some scholars used the thermogravimetric analysis (TGA) technique to measure the adsorption isotherms [6]. Compared with the volumetric method, TGA loads a smaller sample amount into the setup; the magnetic suspension balance mounted in the TGA setup is capable of measuring the weight change down to 1 μ g, rendering the TGA technique more accurate than the volumetric method. However, the adsorption isotherms directly measured by TGA technique are excess adsorption isotherms, which neglects the adsorbed-phase volume and thereby underestimates the total adsorption amount. The density of the adsorption phase is commonly used to correct the excess adsorption isotherms, yielding the absolute adsorption isotherms. In the adsorption phase, gas molecules are in an adsorbed state; to our knowledge, few efforts are dedicated to quantifying the density of the adsorption phase. Previously, constant density values are normally used to pragmatically represent the density of the adsorption phase. Dubinin (1960) [10] suggested that the density of the adsorption phase is a constant value which correlates with the van der Waals constant b . Later, the density of adsorption phase is argued to be equal to the liquid adsorbate density [5,11,12]. Li et al. (2002) [13] compared the aforementioned methods and claimed that the density of the adsorption phase is a function of the system temperature, but its value approaches that proposed by Dubinin (1960) [10]. Recently, with molecular simulations, Ambrose et al. (2012) [14] suggested that the density of the adsorption phase correlates with the system temperature, pressure, and pore size. Actually, fluids in confined space are strongly affected by fluid/pore-surface interactions, especially in shale samples which are usually abundant in nanoscale pores. It is, thereby, of critical importance to precisely capture the density of the adsorption phase in order to more accurately determine the absolute adsorption isotherms.

The objectives of this study are multifold: (1) to use GCMC simulations to capture the *in-situ* density distribution in carbon-slit pores under the effects of the system pressure, temperature, and pore size; (2) to determine the absolute adsorption/desorption isotherms of hydrocarbons on shale samples by knowing the *in-situ* density of the adsorption phase; and (3) to further analyze and compare the characteristics of the absolute adsorption/desorption isotherms of CH_4 and $n-C_4H_{10}$. As part of a comprehensive study on the adsorption/desorption behavior of hydrocarbons in shale reservoirs, we measure the adsorption/desorption isotherms of CH_4 and $n-C_4H_{10}$ on two shale samples using the TGA technique, and then determine the absolute adsorption/desorption isotherms based on GCMC simulations. CH_4 is selected with the consideration that CH_4 is the most abundant component in shale gas or gas condensate, while $n-C_4H_{10}$ adsorption/desorption isotherms are measured to represent the adsorption/desorption behavior of heavier hydrocarbons in shale reservoirs.

2. Experimental section

2.1. Materials and shale sample preparation

The purities of CH_4 and $n-C_4H_{10}$ (Chongqing Tianke Gas Company, China) used in this study are 99.999 mol% and 99.998 wt%, respectively. The uncertainty of the adsorption/desorption measurements as a result of the gas purities can be negligible. Two shale samples, labeled with #1 and #2, are retrieved from the Longmaxi formation located at the depth of 3836 m and 1562 m, respectively, in the southeastern of Sichuan Basin (China). The temperature of the Longmaxi formation is in the range of 355.15–383.15 K and the pressure of this formation is in the range of 100–450 bar. The two shale samples are selected with different TOC contents to clarify the effect of TOC content on the adsorption capacity of hydrocarbons. In this experiment, the shale samples are crushed into small particles with diameters in the range of 1.00–1.18 mm (US Mesh 16–18). Then, to remove the moisture and *in-situ* gas, the shale particles are placed in an oven at 423.15 K, and being vacuumed for 48 h. Prior to their use in the adsorption/desorption measurements, the shale samples are stored in a zip-locked bag to avoid oxidation and water uptake.

2.2. Characterization of shale sample

This section presents the procedures used to characterize the shale samples as well as the characterization results. Various techniques, including the TOC measurement, the scanning electron microscopy (SEM), and the N_2 adsorption/desorption test are adopted to characterize the shale samples.

The TOC content of two shale samples is measured by a combustion elemental analyzer. In this measurement, the organic carbon in shale samples are sparged with oxygen, forming carbon dioxide; then the TOC content is determined by detecting the amount of the carbon dioxide with the non-dispersive infrared detector. The TOC contents of the two shale samples are shown in Table 1. We observe shale sample #1 has a higher TOC content of 3.71 wt%, 3.78 times of that in shale sample #2. The measured TOC contents are in good agreement with the reported values for Longmaxi shale which range from 0.52 to 6.05 wt% [2].

The Hitachi TM-300 SEM setup is used to characterize the surface morphology at an accelerating voltage of 20.0 kV. Prior to scanning, shale surface is polished with argon ion. Subsequently, the polished shale surface is coated with a golden film with a thickness of 10 nm to improve the conductivity. Fig. 1 shows the FE-SEM images taken on the two shale samples. We then further conduct the energy-dispersive X-ray spectroscopy (EDX) analysis on the chosen points “a” and “b” in shale samples #1 and #2, respectively, as marked in Fig. 1. Fig. 2 shows the EDX test results. As seen from Fig. 2, a high concentration of carbon element is present at both sites, indicating that organic matter, i.e., kerogen, is residing in both sites. It can be also seen from Fig. 1 that the kerogen is surrounded by mesopores, which is a typical characteristic observed for kerogen in shale.

Pore size distribution and Brunauer-Emmett-Teller (BET) surface area [4] are characterized by the N_2 adsorption/desorption tests conducted with the Autosorb iQ-Chemisorption & Physi-adsorption Gas Adsorption Analyzer (Quantachrome Instruments, USA). Measured under a wide range of testing pressure, N_2 adsorption isotherms can characterize pore size distributions (PSD) in the micro-, meso- and

Table 1
TOC contents and BET surface areas of the two shale samples used in this study.

Shale sample No.	TOC content (wt%)	R_o (%)	BET surface area (m^2/g)
#1	3.71	2.35	2.98
#2	0.98	1.82	2.06

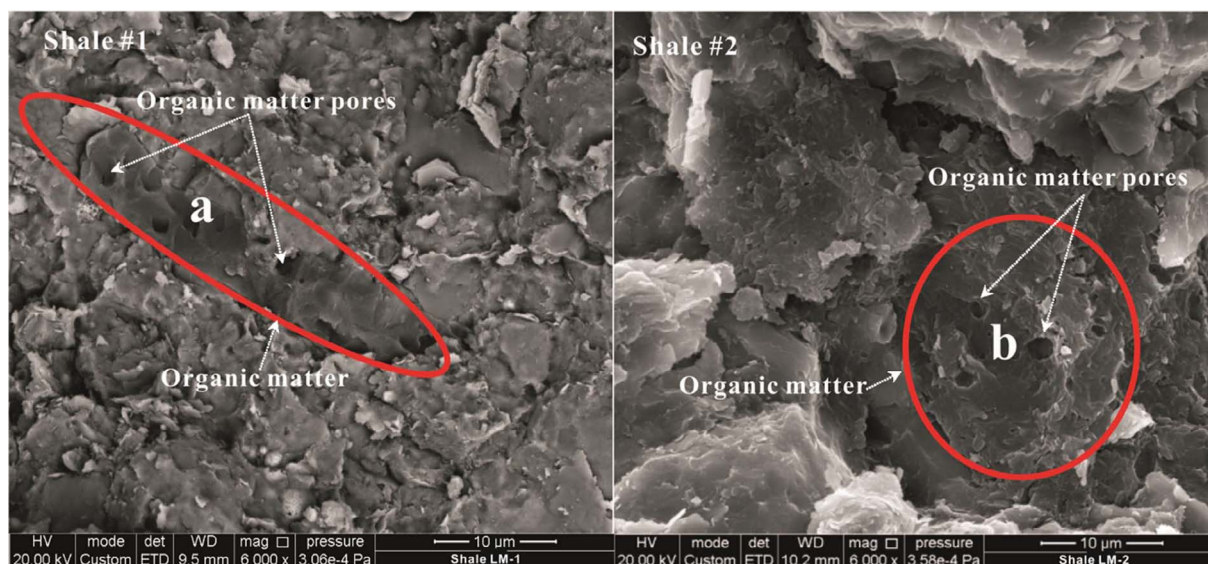


Fig. 1. The FE-SEM images of the two shale samples. Energy-dispersive X-ray spectroscopy (EDX) analysis has been conducted at the sites marked by “a” and “b”.

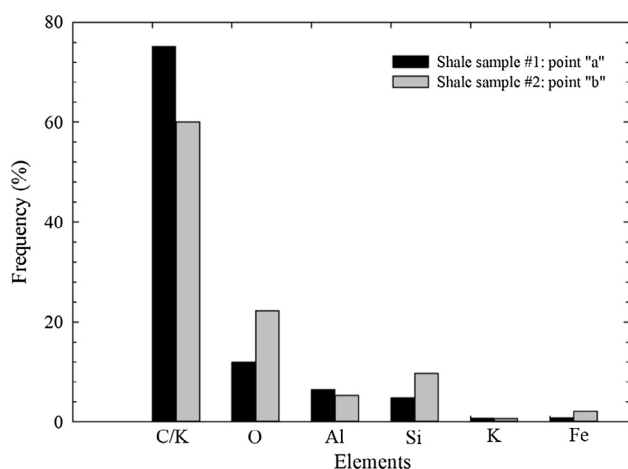


Fig. 2. Energy-dispersive X-ray spectroscopy (EDX) analysis results for points “a” and “b” shown in Fig. 1.

macro-porosity range (approximately 0.5–200 nm) [15]. Therefore, in view of the nature of our shale samples, we select N_2 adsorption isotherm to obtain the PSD of two shale samples. Fig. 3 presents the pore size distribution of the two shale samples as obtained by analyzing the N_2 isotherm data measured at 77.0 K with the non-local density functional theory (NLDFT). The whole region of micro- and mesopores can be properly characterized by this method [16]. But this method also suffers from the following drawbacks: the networking effects and transition from the models of independent pores to the pore networks cannot be addressed [16]. Furthermore, the swelling effect caused by adsorption is not considered in the NLDFT method [16]. The dominant pore size of shale sample #1 is around 4.2 nm, while the dominant pore size of shale sample #2 is around 3.3 nm. Shale sample #1 possesses more mesopores (2–50 nm) and macropores (larger than 50 nm) than shale sample #2, indicating a higher thermal maturity of the organic matter in shale sample #1. We further measure the thermal maturity (R_o) value for each shale sample; the R_o value can represent the thermal maturity of organic matter in shale samples. As shown in Table 1, the R_o values for shale samples # 1 and #2 are 2.35% and 1.82%, respectively, which validates our former statement. As measured in this study, the BET surface area obtained for shale sample #1 is higher than that for shale sample #2.

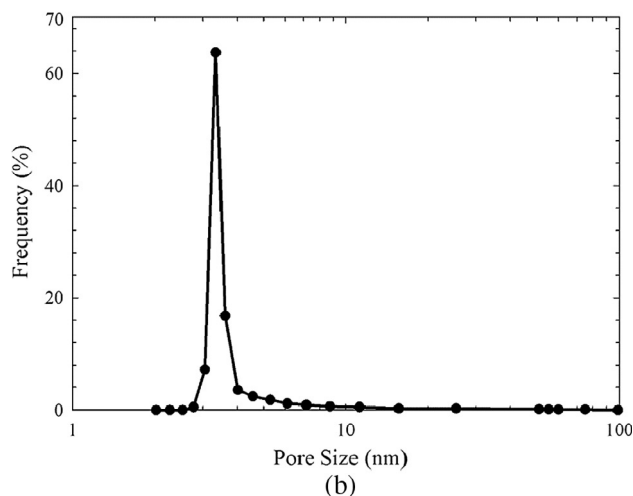
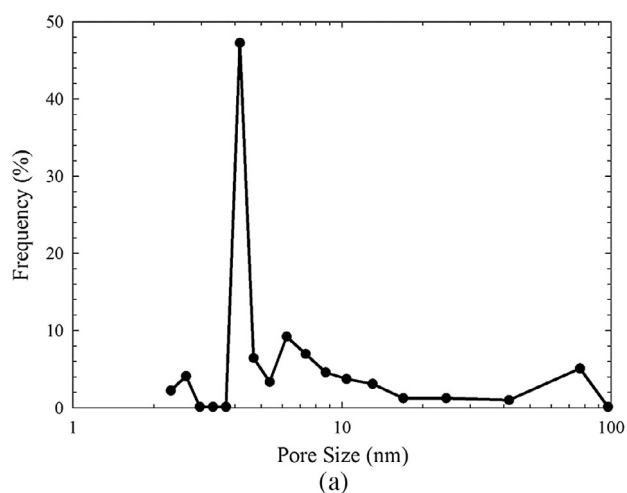


Fig. 3. Pore size distributions of (a) shale sample #1 and (b) shale sample #2 as obtained from N_2 adsorption/desorption test.

2.3. Excess and absolute adsorption/desorption

We measure the excess adsorption/desorption isotherms of CH_4 and $n-C_4H_{10}$ using a thermogravimetric analyser (TGA) (IEA-100B, Hiden

Isochema Ltd., U.K). The key component of TGA is a magnetic suspension balance with 1.0 μg accuracy in weight measurement. In this study, the test pressures are set up to 50 bar for CH_4 and up to 2 bar for $n\text{-C}_4\text{H}_{10}$, respectively, while the test temperatures are set at 303.15, 333.15, 368.15, and 393.15 K. An electrical heater is used to maintain a constant temperature during the adsorption/desorption measurements. It should be noted that 2 bar is the highest pressure we can reach due to the low vapor pressure of $n\text{-C}_4\text{H}_{10}$ at room temperature. Each test is repeated twice to make sure the measured results are reliable and reproducible. The maximum deviation between two consecutive runs is found to be less than $\pm 1.56\%$.

With TGA technique, the measured excess adsorption uptake (M_{ex}) is obtained by [6],

$$M_{ex} = M_a - \rho V_a = M_{app} - (M_s + M_{sc}) + \rho(V_s + V_{sc}) \quad (1)$$

where M_a is the adsorbed uptake on the shale sample, which is defined as the absolute adsorption uptake (M_{ads}), kg; ρ is the bulk gas density, kg/m^3 ; V_a is the adsorption-phase volume, m^3 ; M_{app} is the apparent weight measured by TGA, kg; M_s and M_{sc} are the weight of shale sample and the weight of the sample container, respectively, kg; and $(V_s + V_{sc})$ is the total volume of the shale sample and the sample container, m^3 .

It has been found that, when pore size is large enough, the gas density in the pore center approaches that in bulk [14]. Thereof, in nanopores, the distribution of CH_4 or $n\text{-C}_4\text{H}_{10}$ molecules can be divided into free-gas region and adsorption-phase region. Fig. 4 schematically shows the absolute adsorption uptake, the excess adsorption uptake, the free-gas region, and the adsorption-phase region in a nanopore. As shown in Fig. 4, the density of the adsorption phase (ρ_{ads}) is higher than the bulk free-gas phase density (ρ). The green area depicted in Fig. 4 shows the absolute adsorption. With the knowledge of the density of the adsorption phase and absolute adsorption uptake (M_{ads}), the adsorption-phase volume (V_a) can be calculated using the following equation,

$$V_a = \frac{M_{ads}}{\rho_{ads}} \quad (2)$$

Therefore, the actual adsorbed amount on the shale sample, i.e., absolute adsorption uptake, can be obtained by,

$$M_{ads} = \frac{M_{ex}}{1 - \frac{\rho}{\rho_{ads}}} \quad (3)$$

Thereof, the key to obtain an accurate absolute adsorption uptake is to accurately calculate the density of the adsorption phase. It is known that the density of the adsorption phase is a function of system pressure,

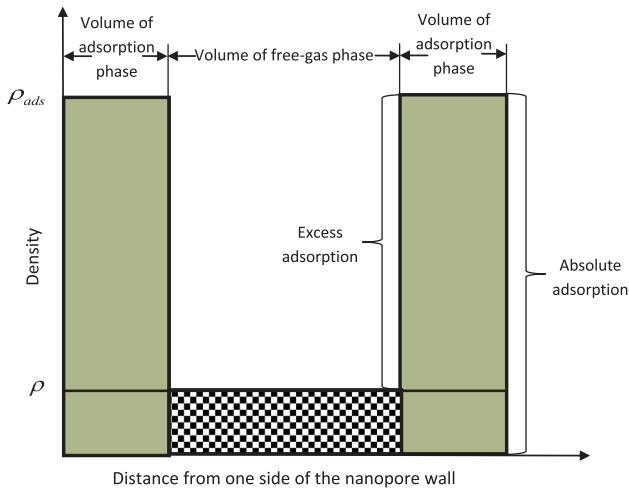


Fig. 4. Schematic of the absolute adsorption and excess adsorption in nanopores. ρ_{ads} is the density of the adsorption phase, and ρ is the density of the free-gas phase, which is equal to the bulk gas density.

temperature, and pore size [14]. However, in previous works, the density of the adsorption phase was provided as a constant which was either calculated from van der Waals constant b [10] or obtained from the liquid density [5,11,12]. From a nanopore-scale perspective, molecular simulations can faithfully capture the properties of the adsorption phase over a wide pressure and temperature range due to the consideration of fluid/pore-surface interactions. In this study, we calculate the density of the adsorption phase using the GCMC simulations.

2.4. GCMC simulations

Within grand canonical (GC) ensemble, the entire system has fixed volume (V), temperature (T) and chemical potential (μ). Since the number of molecules in the system fluctuates during the simulations, the average number of molecules in the ensemble is fully determined by the chemical potential.

In our model, the united atom model [17] is used to simulate different hydrocarbon molecules. The modified Buckingham exponential-6 intermolecular potential [18] is applied to describe non-bonded site-site interactions among functional groups on different molecules, as well as among functional groups belonging to the same molecule separated by more than three bonds. The pairwise interaction potential $U(r)$ for the non-bonded site-site interactions is given as [18],

$$U(r) = \begin{cases} \frac{\epsilon}{1 - \frac{6}{\alpha}} \left[\frac{6}{\alpha} \exp\left(\alpha \left[1 - \frac{r}{r_m}\right]\right) - \left(\frac{r_m}{r}\right)^6 \right], & r > r_{max} \\ \infty, & r < r_{max} \end{cases} \quad (4)$$

where r is the inter-particle separation distance, r_m is the radial distance at which $U(r)$ reaches a minimum, and the cutoff distance r_{max} is the smallest radial distance for which $dU(r)/dr = 0$ [19]. Since the original Buckingham exponential-6 potential can be negative at very short distances, the cutoff distance is thus defined to avoid negative potentials [18]. The radial distance at which $U(r) = 0$ is defined as σ . The values of the exponential-6 parameters ϵ , σ and α are 129.63 K, 0.3679 nm, and 16, respectively, for the methyl group ($-\text{CH}_3$), 73.5 K, 0.4 nm, and 22, respectively, for the methylene group ($-\text{CH}_2-$), and 160.3 K, 0.373 nm, 15, respectively, for CH_4 [19]. The cross parameters are determined by the following combining rules [19],

$$\sigma_{ij} = \frac{1}{2}(\sigma_i + \sigma_j) \quad (5)$$

$$\epsilon_{ij} = (\epsilon_i \epsilon_j)^{1/2} \quad (6)$$

$$\alpha_{ij} = (\alpha_i \alpha_j)^{1/2} \quad (7)$$

The bond lengths for $\text{CH}_3\text{-CH}_2$ and $\text{CH}_2\text{-CH}_2$ are taken as 0.1687 nm and 0.1535 nm, respectively. The torsion potential ($U_{tor}(\varphi)$) is expressed as [20],

$$U_{tor}(\varphi) = V_0 + \frac{V_1}{2}(1 + \cos\varphi) + \frac{V_2}{2}(1 - \cos 2\varphi) + \frac{V_3}{2}(1 + \cos 3\varphi) \quad (8)$$

where φ is the torsional angle from equilibrium, V_0 , V_1 , V_2 , and V_3 are 0, 355.03, -68.19 , and 791.32 K, respectively. The bond bending potential $U_{bend}(\theta)$ is calculated by [21],

$$U_{bend}(\theta) = \frac{K_\theta}{2}(\theta - \theta_{eq})^2 \quad (9)$$

where parameter K_θ is equal to 62500 K/rad², θ is the bond angle from equilibrium, and θ_{eq} is the equilibrium bond angle (114°).

It has been found that the higher organic carbon content enables hydrocarbons to be more apt to adsorb on shale surface [22]. Thereby, in this model, nanopores are selected as slit geometry with smooth and structureless carbon surfaces. 10-4-3 Steele potentials are used to describe the fluid-pore surface interactions φ_{wf} [23],

$$\varphi_{wf}(z) = 2\pi\rho_w\varepsilon_{wf}\sigma_{wf}^2\Delta\left[\frac{2}{5}\left(\frac{\sigma_{wf}}{z}\right)^{10} - \left(\frac{\sigma_{wf}}{z}\right)^4 - \frac{\sigma_{wf}^4}{3\Delta(0.61\Delta + z)^3}\right] \quad (10)$$

where z is the distance of the fluid particle from the pore surface, ρ_{wf} is the density of carbon atom per unit surface area of the graphite layer (114 nm^{-3}), The molecular parameters of an atom in the graphite layer are $\varepsilon_{wf} = 28\text{K}$, and $\sigma_{wf} = 0.3345\text{nm}$ [24], and Δ is the spacing between two adjacent graphene layers (0.335 nm), respectively. The external potential ψ in a slit pore is given as [23],

$$\psi(z) = \varphi_{wf}(z) + \varphi_{wf}(W-z) \quad (11)$$

where W is the size of the slit pore.

In each MC cycle, a trial random displacement is applied to all CH_4 molecules; with equal probability, a CH_4 molecule is randomly removed from or inserted into the simulations box depending on the chemical potential of CH_4 . For simulations of $n\text{-C}_4\text{H}_{10}$ molecules in slit pores, in addition to the MC moves as mentioned above, a trial random rotation is applied to all $n\text{-C}_4\text{H}_{10}$ molecules. We use a configurational-biased GCMC algorithm to insert and remove $n\text{-C}_4\text{H}_{10}$ molecules [25]. The Widom insertion method [26] is used to obtain the chemical potentials of bulk CH_4 and $n\text{-C}_4\text{H}_{10}$ molecules in canonical ensemble. The PR-EOS [27] is applied to calculate the bulk densities of CH_4 and $n\text{-C}_4\text{H}_{10}$ at given pressure and temperature. The MC moves are implemented by using the Metropolis algorithm [28]. During the simulations, 0.1 million of MC cycles per each adsorbate molecule is required to reach an equilibrium state, while 0.5 million of MC cycles per adsorbate molecule is required to sample the density profiles.

The average density (ρ_{ave}) of component i in carbon-slit pores is expressed as,

$$\rho_{ave} = \frac{\langle N_i \rangle M_i}{VN_A} \quad (12)$$

where $\langle N_i \rangle$ is the ensemble averaged number of molecules of component i in nanopores, V is the volume, M is molecular weight of components i , and N_A is Avogadro constant, 6.022×10^{23} .

3. Results and discussion

In the following section, we first explore the detailed density distributions of pure CH_4 or $n\text{-C}_4\text{H}_{10}$ in single carbon-slit pores using GCMC simulations. Then, we calculate the density of the adsorption phase under given conditions. Such density values are subsequently employed to calibrate the excess adsorption/desorption isotherms of CH_4 and $n\text{-C}_4\text{H}_{10}$ which are directly measured by the TGA apparatus. To our knowledge, it is the first time that adsorption/desorption isotherms of $n\text{-C}_4\text{H}_{10}$ on dried shale are measured.

3.1. Density distributions in nanopores

To calculate the density of the adsorption phase, density distributions in nanopores should be known a priori. We investigate the density distributions of pure CH_4 or $n\text{-C}_4\text{H}_{10}$ in a single carbon-slit pore. The effects of the system pressure, temperature, and pore size are examined. In the GCMC framework, CH_4 molecules are regarded as spherical particles, while $n\text{-C}_4\text{H}_{10}$ molecules are represented considering the orientation and configuration [29].

3.1.1. Effect of system pressure

With molecular simulations, Ambrose et al. (2012) [14] found that the CH_4 adsorption behavior in nanopores is sensitive to changes in pressure. To illustrate the effect of system pressure on adsorption behavior of CH_4 and $n\text{-C}_4\text{H}_{10}$, in Fig. 5, we present the density distributions of CH_4 and $n\text{-C}_4\text{H}_{10}$ in 4.2 nm pore at 368.15 K and different system pressures. It is noted that the 4.2 nm is the dominant pore size of shale sample #1. At all bulk pressure conditions, both CH_4 and $n\text{-C}_4\text{H}_{10}$

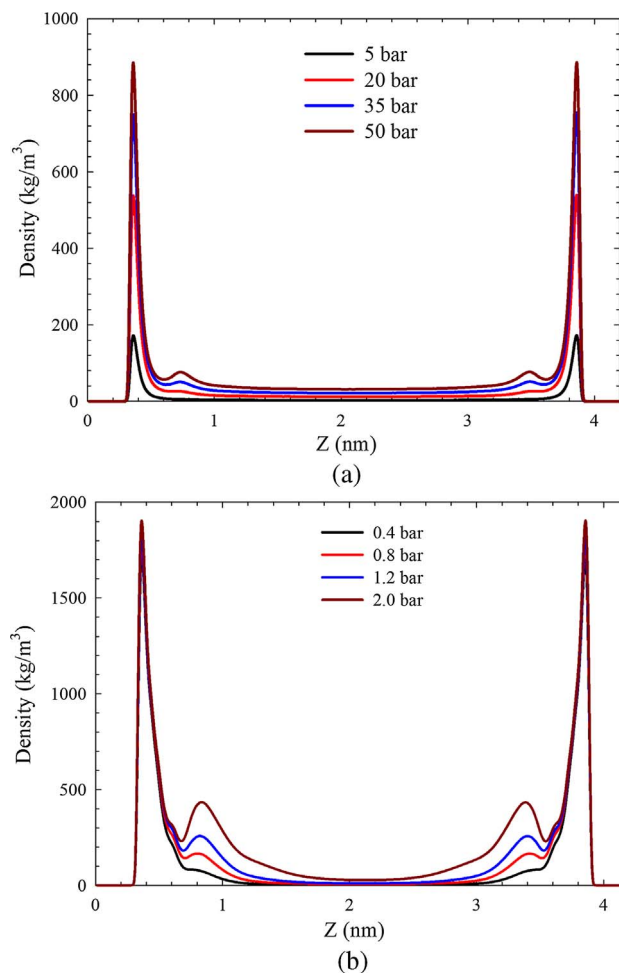


Fig. 5. Density profiles of (a) CH_4 and (b) $n\text{-C}_4\text{H}_{10}$ in the carbon-slit pore of 4.2 nm at 368.15 K and different pressures.

molecules can form one strong adsorption layer and the density in the pore center approaches the bulk density obtained from NIST [30]. Thereby, the gas in the adsorption layer can be considered as the adsorbed gas, while the gas located in the pore center can be taken as the free gas. As for CH_4 , when pressure is larger than 35 bar, a second weak adsorption layer can form in the location adjacent to the first adsorption layer, while $n\text{-C}_4\text{H}_{10}$ forms such a second adsorption layer when system pressure is larger than 0.4 bar. As the bulk pressure increases, the second adsorption layer becomes more pronounced due to the stronger interactions between molecules, as depicted in Fig. 5. Compared with CH_4 , the second adsorption layer of $n\text{-C}_4\text{H}_{10}$ is much stronger due to the stronger molecule/molecule interactions. On the contrary, at a relatively lower pressure, CH_4 or $n\text{-C}_4\text{H}_{10}$ molecules form only one adsorption layer; beyond this adsorption layer, the density is slightly higher than the bulk density, which corresponds to a transition zone in the density profiles [31,34]. Furthermore, we observe that, the density of the adsorption layers of CH_4 and $n\text{-C}_4\text{H}_{10}$ increases with pressure. Therefore, it may not be appropriate to use a constant density value to represent the density of the adsorption phase [5,8].

3.1.2. Effect of system temperature

Fig. 6 shows the density distributions of CH_4 or $n\text{-C}_4\text{H}_{10}$ molecules in a carbon-slit pore of 4.2 nm under different system temperatures. As the system temperature decreases, the density of the adsorption layer increases. However, as temperature increases, adsorption of CH_4 or $n\text{-C}_4\text{H}_{10}$ is significantly suppressed, which is manifested by the drops in the density of the two adsorption layers; this observation is in line with

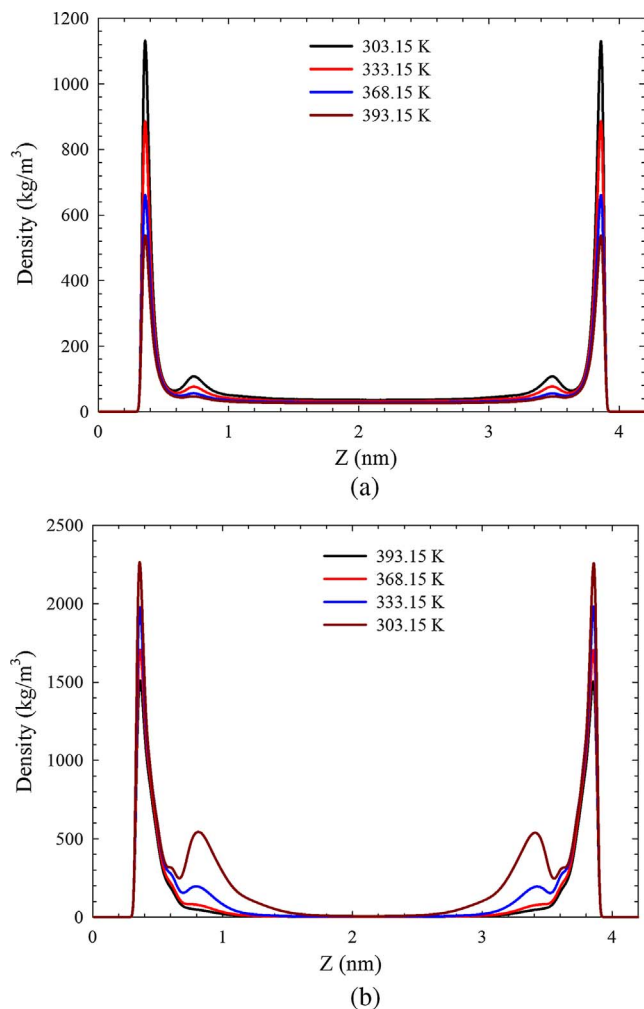


Fig. 6. Density profiles of (a) CH₄ in the carbon-slit pore of 4.2 nm at 50 bar and (b) *n*-C₄H₁₀ in the carbon-slit pore of 4.2 nm at 0.4 bar.

a previous study by Ambrose et al. (2012) [14]. It is due to the weaker fluid/surface interaction at higher temperatures. Comparatively, the density of the two adsorption layers of *n*-C₄H₁₀ is higher than that of CH₄. It is probably because the surface attraction of the carbon wall to *n*-C₄H₁₀ is stronger than that to CH₄, which greatly enhances the adsorption of the heavier alkane, *n*-C₄H₁₀.

3.1.3. Effect of pore size

To reveal the effect of pore size on density profiles, in Fig. 7, we present the density distributions of CH₄ and *n*-C₄H₁₀ molecules in carbon-slit pores of 1.0, 3.3, 4.2, and 5.0 nm. In pores with a size larger than 1.0 nm, CH₄ and *n*-C₄H₁₀ molecules can form two adsorption layers, while, in the 1 nm pore, only one adsorption layer forms on the pore surface due to the limited pore space. In addition, the density in the center of 4.2 nm and 5.0 nm pores approaches the bulk, while the density in the center of 1.0 nm pore is much higher than the bulk value. As the pore size becomes as narrow as 1.0 nm, the packing of molecules in the pore center becomes tighter due to the enhanced attraction forces from the both sides of the pore, leading to the much higher density in the central location of the pore [32,33]. It indicates that there is no free-gas region in such nanopores. It is interesting to observe from Fig. 7 that the density profiles exhibited by CH₄ molecules in the 3.3 nm pore well resemble those in the 4.2 nm and 5.0 nm pores. It implies that once the pore size is larger than a certain value, a change in the pore size will not affect the configuration of the adsorption layers formed by the CH₄ molecules. As for *n*-C₄H₁₀, the density of the free-gas phase in 3.3 nm

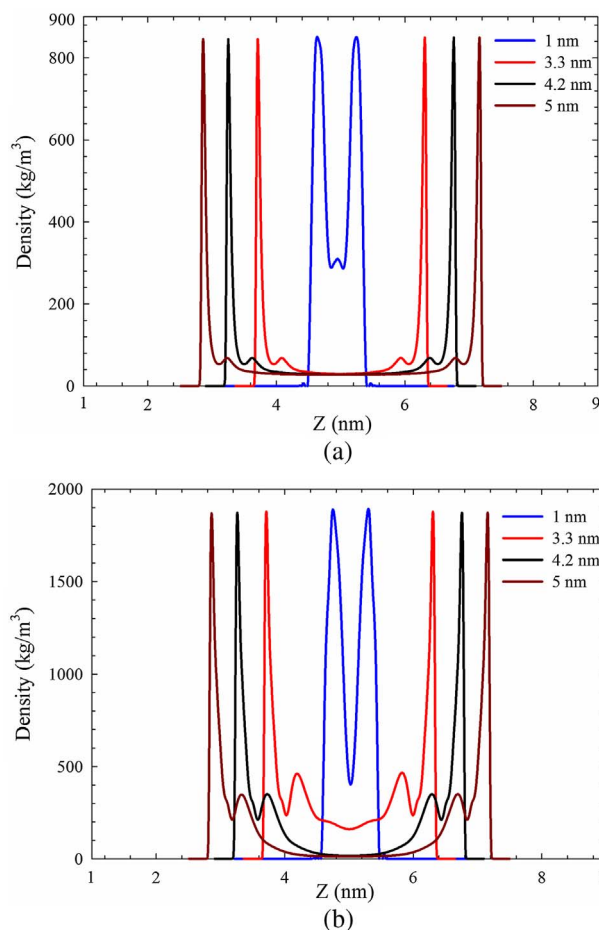


Fig. 7. Density profiles of (a) CH₄ in the carbon-slit pores of 1.0, 3.3, 4.2, and 5.0 nm at 333.15 K and 45 bar and (b) *n*-C₄H₁₀ in the carbon-slit pores of 1.0, 3.3, 4.2, and 5.0 nm at 368.15 K and 1.6 bar.

pore is much higher than those in 4.2 nm and 5.0 nm pores, while the adsorption phase in the 3.3 nm pore well resembles that in the 4.2 nm and 5.0 nm pores. It is clear that the fluid distributions in nanopores can be greatly affected by the pore size. Our results indicate that fluid distributions of CH₄ and *n*-C₄H₁₀ vary in response to the changes in system pressure, temperature, and pore size.

3.1.4. Identification of the adsorption phase

One issue needs to be addressed herein, i.e., how to determine the cutoff distance that separates the free-gas phase and the adsorption phase. As can be observed from Fig. 7, in mesopores (2–50 nm), two adsorption layers are formed, and the density in the pore center approaches that in the bulk. However, in micropores (< 2 nm), only one adsorption layer is formed and the density in the pore center is much higher than bulk. This observation is in line with the previous study by Tian et al. (2017) [34]. As a result, in micropores, it is not justifiable to use the adsorption model in Fig. 4. Considering the two studied shale cores mainly contain mesopores, we thus can define the free-gas phase and the adsorption phase.

We use CH₄ adsorption in 4.2 nm carbon-slit pore as an example to illustrate the methodology for determining the adsorption phase. Fig. 8 presents the density distributions of CH₄ confined in the carbon-slit pore of 4.2 nm at 333.15 K and 50 bar. As shown in this figure, the adsorption phase is defined as the region between *a* (or *a'*) and *b* (or *b'*). The volume between points *a* and *a'* is depicted as the all accessible pore volume of the bulk free gas [34]. Point *b* (or *b'*) is the saddle point between the first adsorption layer and the second weak adsorption layer. The width of the adsorption phase of CH₄ (*ab*), around 0.37 nm, is

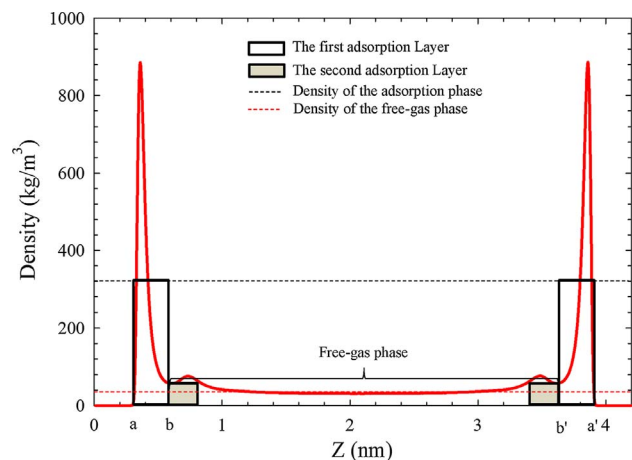


Fig. 8. Density profile of CH₄ in the carbon-slit pore of 4.2 nm at 368.15 K and 50 bar.

similar to the diameter of CH₄ molecule. For *n*-C₄H₁₀, the width of the adsorption phase, around 0.42 nm, is also similar to the diameter of *n*-C₄H₁₀ molecules. It indicates that CH₄ and *n*-C₄H₁₀ generally exhibits single-layered Langmuir adsorption on pore surface under the experimental conditions, which agrees well with the previous studies [35,36]. Using this methodology, we can determine the width of the adsorption phase for CH₄ or *n*-C₄H₁₀ in 3.3 nm and 4.2 nm pores under the experimental pressure/temperature conditions. It is noted that 4.2 and 3.3 nm are the dominant pore sizes of shale sample #1 and #2, respectively. As shown in Fig. 5, it is found that, at a given temperature, the width of the adsorption phase remains almost unchanged as the system pressure increases. However, Fig. 6 shows that, at a given pressure, the width of the adsorption phase increases as the system temperature increases. At a higher temperature, the larger width is probably resulted from the weaker carbon surface/gas interactions.

3.2. Average density of the adsorption phase

By knowing the width of the adsorption phase, the average density of the adsorption phase for CH₄ or *n*-C₄H₁₀ can be thereby calculated by $\rho_{ave} = \int_a^b \rho_{ads}(z) dz / z_{ab}$ (ρ_{ave} is the average density of the adsorption phase; ρ_{ads} is the *in-situ* density of the adsorption phase; and z_{ab} is the distance between *a* and *b*) (See Fig. 8). Figs. 9 and 10 show the average

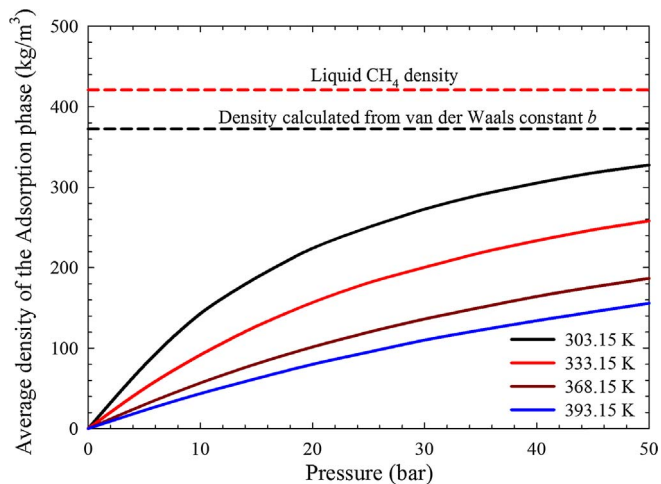


Fig. 9. Average density of the adsorption phase of CH₄ confined in the carbon-slit pore of 3.3 nm and 4.2 nm at different temperatures and pressures. The constant density of liquid CH₄ and the density calculated from van der Waals constant *b* are also shown in this figure. It should be noted that the average density of the adsorption phase of CH₄ confined in 3.3 nm pore is identical to that in the 4.2 nm pore.

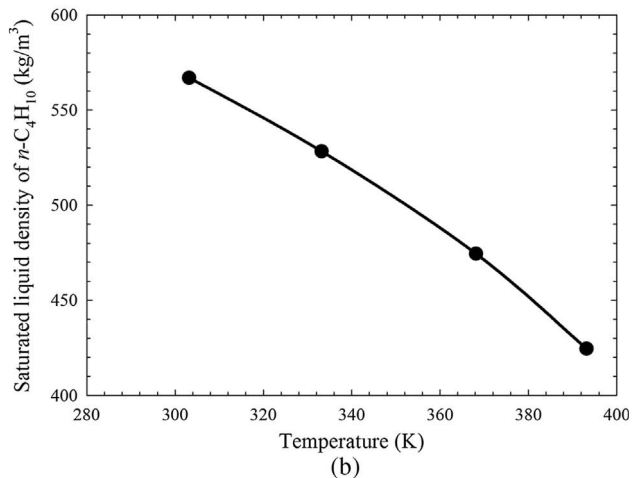
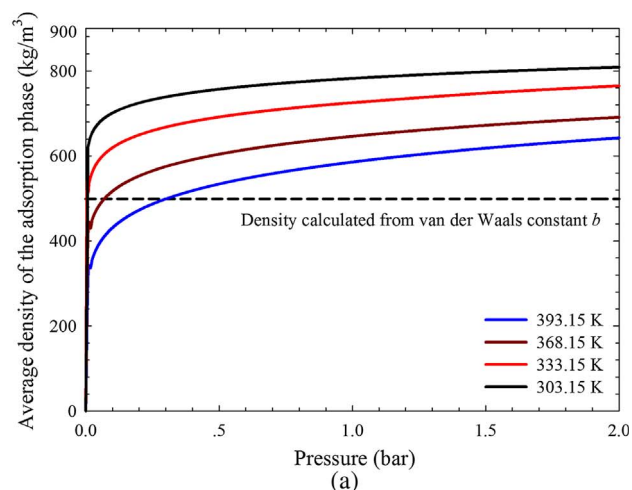


Fig. 10. (a) Average density of the adsorption phase of *n*-C₄H₁₀ confined in the carbon-slit pore of 3.3, and 4.2 nm at different temperatures and pressures. The constant density of liquid *n*-C₄H₁₀ calculated from van der Waals constant *b* is also shown in this figure; (b) Saturated liquid density of *n*-C₄H₁₀ as a function of temperature is calculated by Eq. (13). It should be noted that the average density of the adsorption phase of *n*-C₄H₁₀ confined in 3.3 nm pore is identical to that in the 4.2 nm pore.

density of the adsorption phase for CH₄ and *n*-C₄H₁₀, respectively; we calculate the density of the adsorption phase of CH₄ or *n*-C₄H₁₀ in carbon-slit pores of 3.3 and 4.2 nm at different pressures and temperatures. We find that the average density of the adsorption phase of CH₄ or *n*-C₄H₁₀ in 3.3 nm pore is identical to that in 4.2 nm pore. Furthermore, as for CH₄ and *n*-C₄H₁₀, the average density of the adsorption phase strongly correlates with the system pressure and temperature: it increases as the system pressure increases (or as the system temperature decreases).

Fig. 9 also shows the density of liquid CH₄, 421 kg/m³ [5] and another constant density of CH₄ calculated from the van der Waals constant *b* [10,13,37]. It is noted that the liquid CH₄ density has been extensively used as the density of the adsorption phase to obtain the absolute adsorption isotherms [5] or fit empirical models to the adsorption isotherms [3,37,38]. The constant value of 421 kg/m³ is mostly used. The constant density of CH₄ based on the van der Waals constant *b* is also heavily used to represent the density of the adsorption phase, i.e., 1/*b* [10,13,37]. Fig. 10a also shows the density of liquid *n*-C₄H₁₀ calculated from the van der Waals constant *b*, 502 kg/m³. Since the saturated liquid density of *n*-C₄H₁₀ is known to correlate with system temperature, the following correlation can be used to calculate the saturated liquid density of *n*-C₄H₁₀, as depicted in Fig. 10b [39],

Table 2
Critical properties of $n\text{-C}_4\text{H}_{10}$ used for density calculation [42].

Adsorbate	T_c (K)	P_c (bar)
$n\text{-C}_4\text{H}_{10}$	425.18	37.97

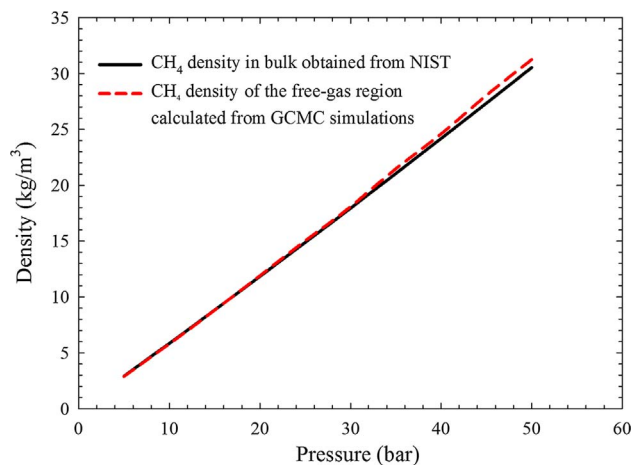


Fig. 11. Comparisons of CH_4 density of the free-gas region at the carbon-slit pore of 4.2 nm at 333.15 K calculated by GCMC simulations with CH_4 density in bulk obtained from NIST.

$$\log_{10}\left(\frac{\rho_{n\text{C}_4\text{H}_{10}}}{1000}\right) = \log_{10}(h) - \log_{10}(l) \left(1 - \frac{T}{T_c}\right)^n \quad (13)$$

where $\rho_{n\text{C}_4\text{H}_{10}}$ is saturated density of $n\text{-C}_4\text{H}_{10}$, kg/m^3 ; T_c is the critical temperature of $n\text{-C}_4\text{H}_{10}$; h , l , and n are coefficients with values of 0.2283, 0.2724, and 0.2863, respectively. The critical pressure and temperature of $n\text{-C}_4\text{H}_{10}$ used are listed in Table 2. It is clear that, as for either CH_4 or $n\text{-C}_4\text{H}_{10}$, the density of the adsorption phase should be a variable which depends on the *in-situ* temperature/pressure, rather than a constant value. As shown in Fig. 8, the free-gas is defined as the region between points b and b' , which covers the second weak adsorption layer. In Fig. 11, we compare the average density of the free-gas region of CH_4 in a 4.2 nm pore calculated by the GCMC simulations with the bulk density from NIST [30]. The average density of the free-gas region for CH_4 is calculated by $\rho_f = \int_b^{b'} \rho(z) dz / z_{bb'}$ (ρ_f is the average density of the free-gas phase; ρ is the *in-situ* density of the free-gas phase; and $z_{bb'}$ is the distance between b and b') (see Fig. 8). Fig. 11 shows the comparative results at 333.15 K, demonstrating that the density values calculated from GCMC simulations is in a good agreement with the NIST data, especially at relatively low pressures. This proves the reliability of the GCMC simulations. But deviation shows up at pressures larger than 30 bar and increases as pressure further increases. Such deviation can be attributed to the presence of the transition zone [34] (See Fig. 5).

3.3. Absolute adsorption/desorption isotherms

Since the measured adsorption/desorption isotherms are surface excess quantities, the density of the adsorption phase is required to transform these excess values to absolute ones. Based on the density of the adsorption phase computed from GCMC simulations, we convert the excess adsorption/desorption isotherms to absolute ones. Figs. 12 and 13 present the converted absolute adsorption/desorption isotherms of CH_4 and $n\text{-C}_4\text{H}_{10}$ on the two shale samples studied. We observe that the absolute adsorption of CH_4 or $n\text{-C}_4\text{H}_{10}$ increases as pressure increases or as temperature decreases. At the same pressure and temperature, $n\text{-C}_4\text{H}_{10}$ has relatively higher adsorption capacity compared to CH_4 ; it is because pore surface shows stronger attractions towards $n\text{-C}_4\text{H}_{10}$

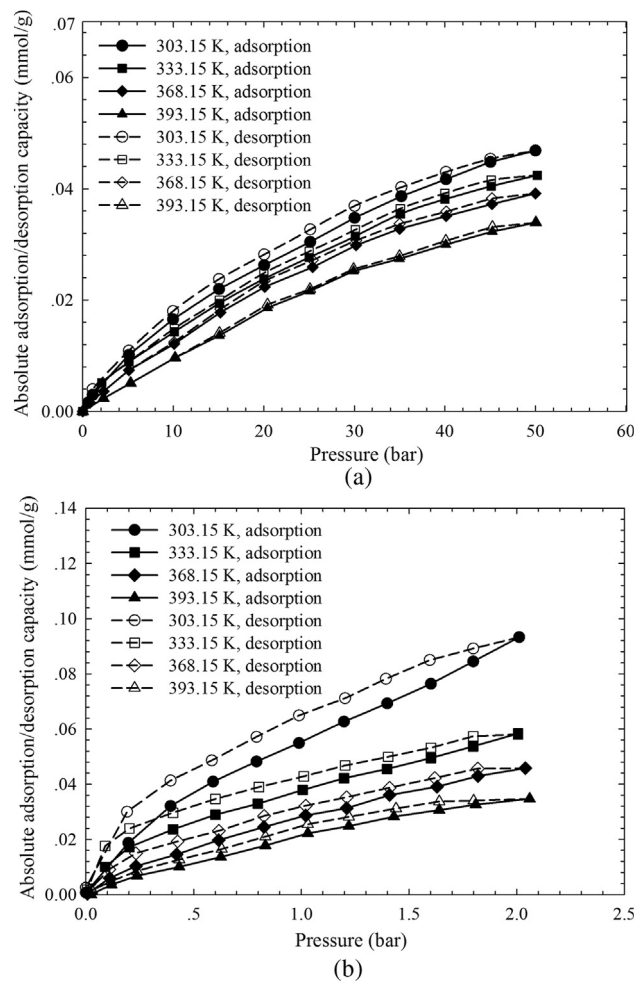


Fig. 12. Absolute adsorption/desorption isotherms of (a) CH_4 and (b) $n\text{-C}_4\text{H}_{10}$ on shale sample #1. These isotherms are obtained by converting the excess adsorption/desorption isotherms based on the average density of the adsorption phase calculated by GCMC simulations.

molecules than CH_4 , indicating a higher affinity of $n\text{-C}_4\text{H}_{10}$ towards shale. In shale reservoirs, the heavier hydrocarbons can be more easily to get adsorbed on the shale surface, forming liquid-phase-like structures and showing stronger storage capacity as the adsorbed state [35].

The difference in the adsorption and desorption isotherms is termed as the hysteresis phenomenon. This hysteresis behavior can be attributed to the capillary condensation taking place in nanopores as pressure changes at a given temperature [35,40]. With density functional theory (DFT), Li et al. (2014) [35] studied the adsorption/desorption hysteresis of pure CH_4 and pure $n\text{-C}_4\text{H}_{10}$ in a single carbon-slit pore and found that the hysteresis phenomenon for pure component only occurs over a small pressure range at a given temperature. The measured results shown in Figs. 12 and 13 show that, however, in a real shale sample, the hysteresis phenomenon for CH_4 or $n\text{-C}_4\text{H}_{10}$ appears over the entire pressure range at a given temperature. The shale samples are porous media containing a series of pores with different sizes. The hysteresis in shale samples is not as sharp as that in a carbon-slit pore, which is probably because: (1) a given shale sample contains a series of pores with different sizes; and (2) hysteresis may appear at different pressures in different pores. As for both CH_4 and $n\text{-C}_4\text{H}_{10}$, the hysteresis phenomenon is getting more pronounced at a lower temperature. Comparatively speaking, $n\text{-C}_4\text{H}_{10}$ exhibits stronger adsorption/desorption hysteresis than CH_4 , which agrees well with the simulation studies based on the use of DFT [35].

Comparing Fig. 12 with 13, we observe CH_4 or $n\text{-C}_4\text{H}_{10}$ exhibits a

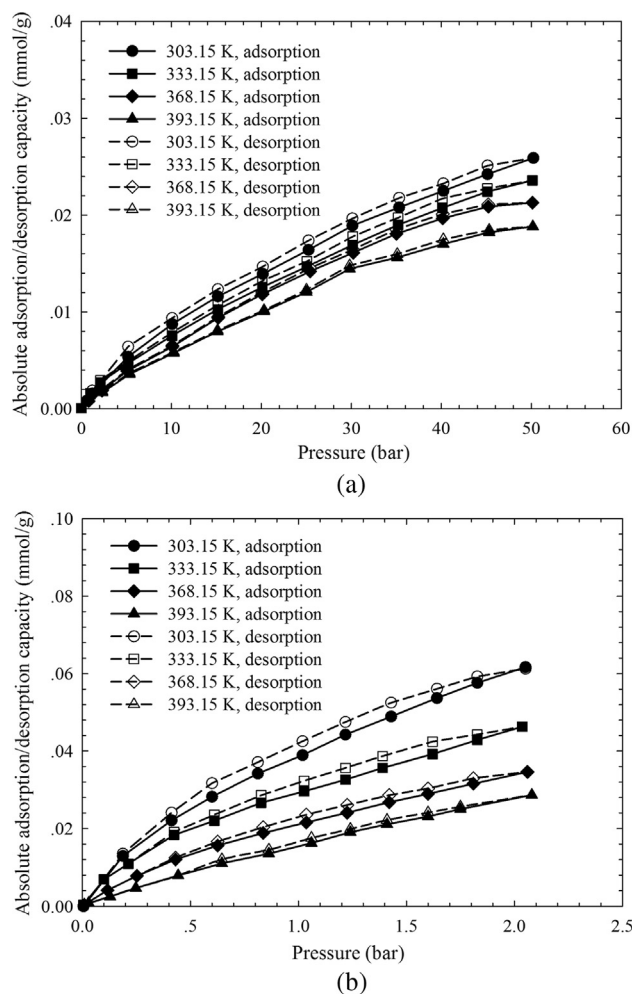


Fig. 13. Absolute adsorption/desorption isotherms of (a) CH_4 and (b) $n\text{-C}_4\text{H}_{10}$ on shale sample #2. These isotherms are obtained by converting the excess adsorption/desorption isotherms based on the average density of the adsorption phase calculated by GCMC simulations.

higher adsorption capacity on shale sample #1 than shale sample #2. Adsorption strongly correlates with the TOC content and surface area in the shale sample [22]. Thereof, such higher adsorption on shale sample #1 may be caused by the higher TOC content (3.17 wt%) and larger BET surface area ($2.98 \text{ m}^2/\text{g}$) than those of shale sample #2 (a TOC content of 0.98 wt% and a BET surface area of $2.06 \text{ m}^2/\text{g}$). However, Xiong et al. (2017) [41] presented that the adsorption capacity does not correlate only with the TOC and surface area but shows a more complex dependence on the petro-physical and mineralogical properties; therefore, to understand the adsorption capacity of CH_4 or $n\text{-C}_4\text{H}_{10}$, more adsorption data should be measured and other factors, e.g., clay minerals, should be considered to understand the adsorption behavior.

In Figs. 14 and 15, we compare the excess adsorption isotherms of CH_4 and $n\text{-C}_4\text{H}_{10}$ against the corresponding absolute adsorption isotherms. As mentioned above, the excess adsorption isotherms are converted to the absolute adsorption isotherms using the *in-situ* density of the adsorption phase which are calculated from GCMC simulations. It can be seen from Figs. 14a and 15a that, as for CH_4 , the absolute adsorption is found to be always higher than the directly measured excess adsorption. A relatively large deviation is found to exist between the absolute adsorption isotherms and the excess adsorption isotherms for CH_4 , which highlights the importance of using accurate density of the adsorption phase to obtain accurate absolute adsorption isotherms for CH_4 . However, as for $n\text{-C}_4\text{H}_{10}$, the absolute adsorption isotherms are almost identical to the excess adsorption isotherms (See

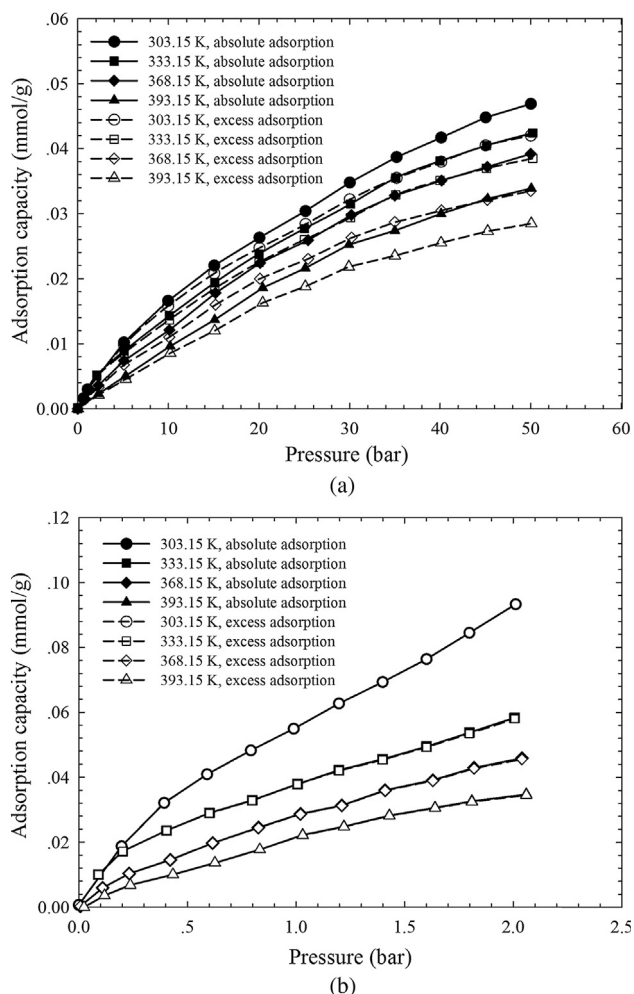


Fig. 14. Comparisons of absolute adsorption isotherms with excess ones on shale sample #1: (a) CH_4 and (b) $n\text{-C}_4\text{H}_{10}$. The absolute adsorption isotherms have been converted from the excess adsorption isotherms based on density of the adsorption phase which is calculated by GCMC simulations.

Figs. 14b and 15b). In this work, we measure the adsorption of $n\text{-C}_4\text{H}_{10}$ on shale samples at pressures only up to 2 bar; under such low pressures, the bulk gas density is far less than the density of the adsorption phase, as seen from Fig. 5b. As a result, the term ρ/ρ_a is a value approaching zero. As such, the denominator in the right hand side of Eq. (3) approaches 1, rendering the absolute adsorption being almost equal to the excess adsorption. This explains why the absolute adsorption isotherms for $n\text{-C}_4\text{H}_{10}$ are almost identical to the excess adsorption isotherms, as shown in Figs. 14b and 15b.

3.4. Comparison of GCMC-based approach with conventional approach

The liquid density and the density calculated from van der Waals constant b are commonly used to approximate the density of the adsorption phase. Herein, the densities calculated from these two conventional approaches are used to convert the measured excess adsorption isotherms to the absolute ones. Thereafter, we compare the absolute adsorption isotherms converted by the two conventional approaches with those calculated from the GCMC simulations. Fig. 16 compares the absolute adsorption capacity of CH_4 and $n\text{-C}_4\text{H}_{10}$ on shale sample #1 calculated by GCMC-based approach against that calculated by using the liquid density of CH_4 or $n\text{-C}_4\text{H}_{10}$, while Fig. 17 compares the absolute adsorption capacity of CH_4 and $n\text{-C}_4\text{H}_{10}$ on shale sample #1 calculated by GCMC-based approach against that calculated using the van der Waals constant b . As can be seen from Figs. 16b and 17b, as

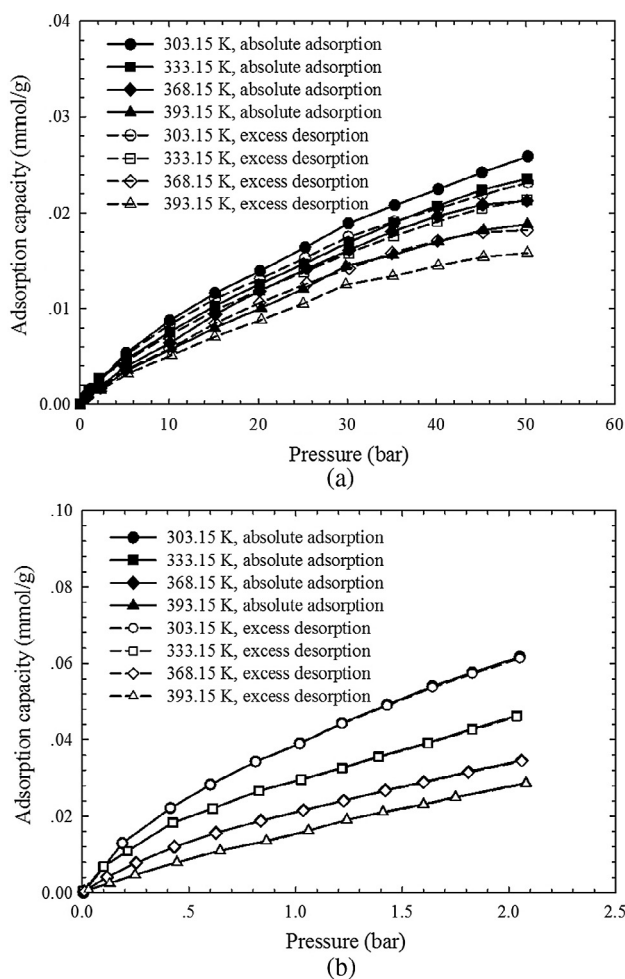


Fig. 15. Comparisons of absolute adsorption isotherms with excess ones on shale sample #2: (a) CH₄ and (b) *n*-C₄H₁₀. The absolute adsorption isotherms have been converted from the excess adsorption isotherms based on density of the adsorption phase which is calculated by GCMC simulations.

for *n*-C₄H₁₀, the conventional approaches and the GCMC-based approach provide almost the same conversion results. However, as seen from Figs. 16a and 17a, the conventional approach tends to underestimate the absolute adsorption for CH₄. These aforementioned findings highlight the importance of obtaining an accurate estimation of the adsorption-phase density, especially when one wants to accurately evaluate the total amount of gas-in-place in shale gas reservoirs.

4. Conclusions

In this study, we measure the excess adsorption/desorption isotherms of CH₄ and *n*-C₄H₁₀ on two shale samples. Density distributions of CH₄ and *n*-C₄H₁₀ in nanopores are investigated with the GCMC simulations. A pragmatic approach is used to estimate the adsorption-phase density based on the GCMC simulations, finding that the density of the adsorption phase correlates with system pressure, temperature, and pore size. Consequently, the *in-situ* density of the adsorption phase is used to convert the excess adsorption/desorption isotherms to the absolute adsorption/desorption isotherms. The following conclusions can be drawn:

- The GCMC simulations show that the density distributions of CH₄ or *n*-C₄H₁₀ vary in response to the changes in system pressure, temperature, and pore size. The calculated density of the adsorption phase of CH₄ is always lower than the liquid CH₄ density and, at high pressures, the density of the adsorption phase is found to be

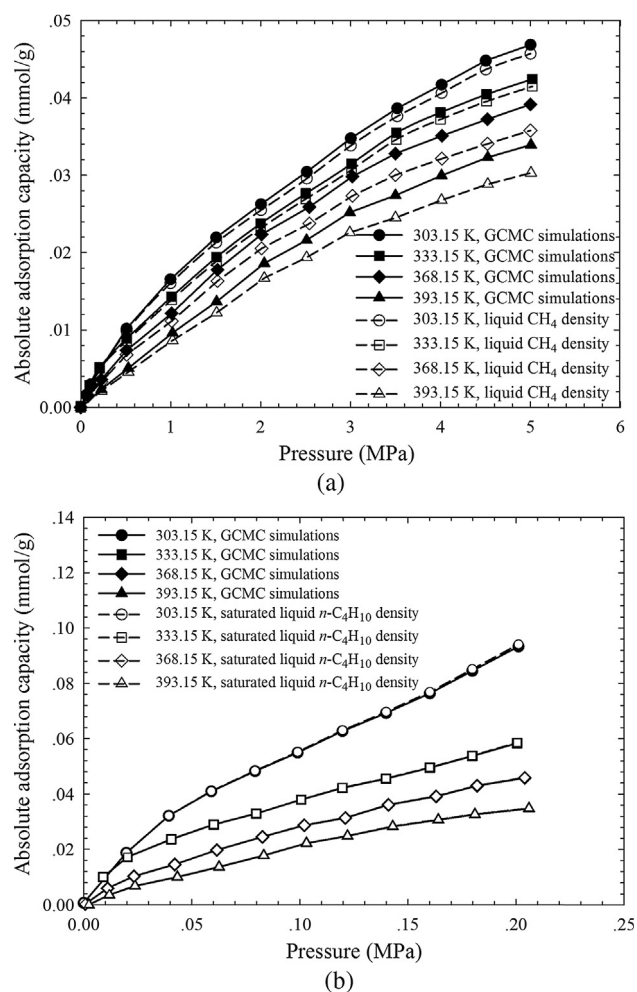


Fig. 16. Comparisons of absolute adsorption capacity of (a) CH₄ and (b) *n*-C₄H₁₀ on shale sample #1 calculated by GCMC-based approach with that obtained by the liquid density of CH₄ or *n*-C₄H₁₀.

very close to but never equal or greater than the liquid phase density. The calculated density of the adsorption phase of *n*-C₄H₁₀ can be higher than the liquid *n*-C₄H₁₀ density.

- More obvious adsorption/desorption hysteresis and higher adsorption capacity are observed for *n*-C₄H₁₀ than CH₄. This indicates a higher affinity of *n*-C₄H₁₀ towards the two shale samples.
- GCMC simulations can faithfully capture the *in-situ* density of the adsorption phase by better honoring the carbon pore-surface/gas interactions. Compared with the GCMC-based approach, the conventional approaches, on the basis of using a constant density for the adsorption phase, are appropriate for obtaining the absolute adsorption isotherms for *n*-C₄H₁₀, but tend to significantly underestimate the absolute adsorption isotherms for CH₄.
- The adsorption capacity of CH₄ or *n*-C₄H₁₀ on the shale sample #1 is much higher than that on the shale sample #2, which may be caused by the fact that the shale sample #1 has a higher TOC content and a larger BET surface area.

Although this work provides an alternative method to correct the measured excess adsorptions, there are still some issues that remain to be addressed in future work. Firstly, we only measure the adsorption isotherms at the pressures up to 2 bar for *n*-C₄H₁₀ considering the low vapor pressure of *n*-C₄H₁₀ at room temperature. If possible, the testing pressures should be as high as the reservoir conditions to make the measurements more realistic. Secondly, we only measure the adsorption/desorption isotherms for CH₄ and *n*-C₄H₁₀. Similar measurements

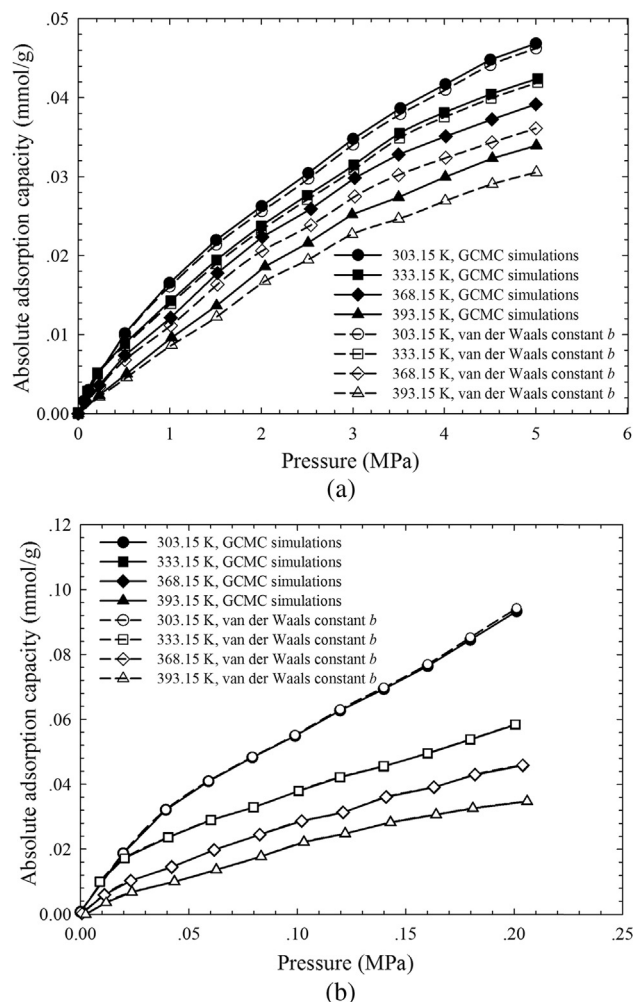


Fig. 17. Comparisons of absolute adsorption capacity of (a) CH₄ and (b) n-C₄H₁₀ on shale sample #1 calculated by GCMC-based approach with that obtained by the density calculated by van der Waals constant *b*.

should be also done on other components, e.g., C₂H₆ and C₃H₈, which may also exist in shale reservoirs. Thirdly, shale gas is a multi-component mixture, and different components can exhibit different adsorption behavior on shale, leading to the selective adsorption behavior for gas mixtures. Therefore, excess adsorption isotherms of gas mixtures should be measured, and new techniques should be developed accordingly to correct the excess values and obtain the accurate absolute adsorption of gas mixtures on shale.

Acknowledgments

The authors greatly acknowledge a Discovery Grant from the Natural Sciences and Engineering Research Council (NSERC) of Canada to H. Li (NSERC RGPIN 05394) and financial support by Open Fund (PLC201606) of State Key Laboratory of Oil and Gas Reservoir Geology and Exploitation (Chengdu University of Technology, China) to H. Li, a NSERC Discovery Grant to Z. Jin (NSERC RGPIN-2017-05080) and a China Scholarship Council (CSC) PhD Scholarship to Y. Liu (201406450028). We are especially indebted to Dr. Hao Zhang from Chengdu University of Technology for his assistance in conducting the adsorption experiments. This research was enabled in part by support provided by Westgrid (www.westgrid.ca) and Compute Canada (www.computeCanada.ca).

References

- [1] Ross DJK, Bustin RM. The importance of shale composition and pore structure upon gas storage potential of shale gas reservoirs. *Mar Pet Geol* 2009;26:916–27.
- [2] Wu Y, Fan T, Jiang S, et al. Methane adsorption capacities of the lower paleozoic marine shales in the yangtze platform, South China. *Energy Fuels* 2015;29:4160–7.
- [3] Gasparik M, Ghanizadeh A, Bertier P, et al. High-pressure methane adsorption isotherms of black shales from the Netherlands. *Energy Fuel* 2012;26:4995–5004.
- [4] Duan S, Gu M, Du X, et al. Adsorption equilibrium of CO₂ and their mixture on sichuan basin shale. *Energy Fuels* 2016;30:2248–56.
- [5] Wang Y, Zhu Y, Liu S, et al. Methane adsorption measurements and modeling for organic-rich marine shale samples. *Fuel* 2016;172:301–9.
- [6] Wang Y, Tsotsis TT, Jessen K. Competitive adsorption of methane/ethane mixtures on shale: measurements and modeling. *Ind Eng Chem Res* 2015;54:12187–95.
- [7] Pedram EO, Hines AL, Cooney DO. Adsorption of light hydrocarbons on spent shale produced in a combustion retort. *Chem Eng Commun* 1984;27:181–91.
- [8] Heller R, Zoback M. Adsorption of methane and carbon dioxide on gas shale and pure mineral samples. *J Unconv Oil Gas Res* 2014;8:14–24.
- [9] Gasparik M, Bertier P, Gensterblum Y, et al. Geological controls on the methane storage capacity in organic-rich shales. *Int J Coal Geol* 2014;123:34–51.
- [10] Dubinin MM. The potential theory of adsorption of gases and vapors for adsorbents with energetically nonuniform surfaces. *Chem Rev* 1960;60(2):235–41.
- [11] Menon PG. Adsorption at high pressures. *J Phys Chem* 1968;72:2695–6.
- [12] Tsai MC, Chen WN, Cen PL, et al. Adsorption of gas mixture on activated carbon. *Carbon* 1985;23(2):167–73.
- [13] Li M, Gu A, Lu X, et al. Determination of the adsorbate density from supercritical gas adsorption equilibrium data. *Carbon* 2002;41:579–625.
- [14] Ambrose RJ, Hartman RC, Diaz-Campos M, et al. Shale gas-in-place calculations part i: new pore-scale considerations. *SPE J* 2012;17(1):21–29.
- [15] Groen JC, et al. Pore size determination in modified micro- and mesoporous materials. pitfalls and limitations in gas adsorption data analysis. *Micropor Mesopor Mat* 2003;60:1–17.
- [16] Landers J, Gor GY, Neimark AV. Density functional theory methods for characterization of porous materials. *Colloids Surf A Physicochem Eng Aspects* 2013;437:3–32.
- [17] Martin MG, Siepmann JI. Transferable potentials for phase equilibria. 1. United-atom description of n-alkanes. *J Phys Chem B* 1998;102(14):2569–77.
- [18] Errington JR, Panagiotopoulos AZ. A new intermolecular potential model for the n-alkane homologous series. *J Phys Chem B* 1999;103(30):6314–22.
- [19] Singh SK, Sinha AK, Deo G, et al. Vapor-liquid phase coexistence, critical properties, and surface tension of confined alkanes. *J Phys Chem C* 2009;113(17):170–80.
- [20] Smit B, Karaborni S, Siepmann JI. Computer simulations of vapor-liquid phase equilibria of n-alkanes. *J Chem Phys* 1995;102(5):2126–40.
- [21] van der Ploeg P, Berendsen HJC. Molecular dynamics simulations of a bilayer membrane. *J Chem Phys* 1982;76(6):3271–6.
- [22] Kim J, Kim D, Lee W, Lee Y, Kim H. Impact of total carbon and specific area on the adsorption capacity in horn river shale. *J Petrol Sci Eng* 2017;149:331–9.
- [23] Steele WA. The physical interaction of gases with crystalline solids. I. Gas-Solid energies and properties of isolated adsorbed atoms. *Surf Sci* 1973;36(1):317–52.
- [24] Do DD, Do HD. Adsorption of supercritical fluids in non-porous and porous carbons: analysis of adsorbed phase volume and density. *Carbon* 2003;41:1777–91.
- [25] Hensen EJM, Tambach TJ, Blik A, et al. Adsorption isotherms of water in Li-, Na-, and K-montmorillonite by molecular simulations. *J Chem Phys* 2001;115(7):3322–9.
- [26] Widom B. Some topics in the theory of fluids. *J Chem Phys* 1963;39(11):2808–12.
- [27] Peng D, Robinson DB. A new two-constant equation of state. *Ind Eng Chem Fund* 1976;15(1):59–64.
- [28] Metropolis N, Rosenbluth AW, Rosenbluth MN, et al. Equation of state calculations by fast computing machines. *J Chem Phys* 1953;21(6):1087–92.
- [29] Jin Z, Firoozabadi A. Phase behavior and flow in shale nanopores from molecular simulations. *Fluid Phase Equilib* 2016;430:156–68.
- [30] Lemmon EW, McLinden MO, Friend DG. Thermophysical properties of fluid systems. N.I.S.T. Chemistry WebBook, NIST Standard Reference Database Number 69. Gaithersburg, MD: National Institute of Standards and Technology; 2009.
- [31] Didar, B.R. and Akkutu, I.Y. Pore-size Dependence of Fluid Phase Behavior and Properties in Organic-Rich Shale Reservoirs. *SPE International Symposium on Oilfield Chemistry*. Woodlands, Texas, USA, 2013.
- [32] Liu Y, Wilcox J. Molecular simulations of CO₂ adsorption in Micro- and mesoporous carbons with surface heterogeneity. *Int J Coal Geol* 2012;104:83–95.
- [33] Chen G, Zhang J, Lu S, et al. Adsorption behavior of hydrocarbon on illite. *Energy Fuels* 2016;30:9114–21.
- [34] Tian Y, Yan C, Jin Z. Characterization of methane excess and absolute adsorption in various clay nanopores from molecular simulation. *Sci Rep* 2017;7:12040.
- [35] Li ZD, Jin ZH, Firoozabadi A. Phase behavior and adsorption of pure substances and mixtures and characterization in nanopores structures by density functional theory. *SPE J* 2014;19(6):1096–109.
- [36] Dong X, Liu H, Hou J, Wu K, Chen Z. Phase equilibria of confined fluids in nanopores of tight and shale rocks considering the effect of capillary pressure and adsorption film. *Ind Eng Chem Res* 2016;55:798–811.
- [37] Rexer TFT, Benham MJ, Aplin AC, Thomas KM. Methane adsorption on shale under simulated geological temperature and pressure conditions. *Energy Fuels* 2013;27:3099–109.
- [38] Weniger P, Kalkreuth W, Busch A, et al. High-pressure methane and carbon dioxide sorption on coal and shale samples from the paran basin. *Braz Int J Coal Geol* 2010;84:190–205.
- [39] Yaws CL. *Yaws' Handbook of Thermodynamic and Physical Properties of Chemical Compounds*. New York, NY: Knovel Corporation; 2003.
- [40] Bryan WP. Sorption hysteresis and the laws of thermodynamics. *J Chem Educ* 1987;64(3):209–12.
- [41] Xiong F, Wang X, Amooie N, et al. The shale gas sorption capacity of transitional shales in the ordos basin, NW China. *Fuel* 2017;208:236–46.
- [42] Firoozabadi A. *Thermodynamics and Applications in Hydrocarbon Energy Production*. New York: McGraw Hill; 2016.